Master's Thesis of Engineering

Emulating Mixed-Plasticity in a 2-Terminal Halide Perovskite Artificial Synapse

2단자 할라이드 페로브스카이트 인공 시냅스에서
혼합 가소성 구현

February 2023

Graduate School of Engineering
Seoul National University
Material Science and Engineering Major

Dae-Han Kang

Emulating Mixed-Plasticity
in a 2-Terminal Halide Perovskite
Artificial Synapse

Advisor Tae-Woo Lee

Submitting a master's thesis of
Engineering

February 2023

Graduate School of Engineering
Seoul National University
Material Science and Engineering Major

Dae-Han Kang

Confirming the master's thesis written by
Dae-Han Kang
February 2023

Chair	김 상 범	(Seal)
Vice Chair	이 태 우	(Seal)
Examiner	박 민 혁	(Seal)

Abstract

Achieving an artificial synapse in which short-term plasticity (STP) and long-term plasticity (LTP) operate simultaneously (mixed-plasticity) can provide adaptation to dynamic situation and memory formation at the same time. Therefore, emulating the mixed-plasticity (STP + LTP) in a single device can contribute to the implementation of neuromorphic systems that deal with real-time data. Although there are several devices that the mixed-plasticity is emulated, in such devices, the STP and LTP are governed by a single mechanism. Since controlling the mixed-plasticity by a single mechanism is challenging by the presence of the contradiction issue, to solve this problem, here, we adopted halide perovskite as an active layer of a 2-terminal artificial synapse. Moreover, we introduced ferroelectricity into the halide perovskite active layer through composition component engineering. As a result, in the halide perovskite active layer, we could utilize the halide perovskite's ion and vacancy migration for STP emulation and the introduced ferroelectricity for LTP emulation; 2 separated mechanisms for the reliably and simultaneously operated mixed-plasticity. Through this new approach as above, we could succeed in emulating the reliably and simultaneously operated mixed-plasticity with the halide perovskite artificial synapse while controlling the STP mode and LTP mode

by regulating the presynaptic spike voltage magnitude.

Table of Contents

List of Figures

Chapter 1. Introduction

1.1. Study Background

Brain is an energy-efficient neural network with a high density of nearly

10^{12} neurons and 10^{15} synapses.[1-2] Neurons are channels for transmitting

information in the form of discrete action potentials. Synapses are connection parts

between pre- and post-neurons where data processing and storage simultaneously

happen. The brain overwhelms conventional von Neumann-based computers in

specific areas such as recognition in a dynamic situation and inference of complex

things consuming just 20W.[2] Although it is not yet fully understood how the

compact brain can show the amazing performance, its remarkable ability is thought

to stem from the vast connectivity, the hierarchical structure of synapses, and time-

dependent synaptic functions.[3-4]

Neuromorphic electronics is an attempt to imitate the human's superiority

by emulating the biological neurons and synapses.[5-16] Especially, the most

important point is the emulation of synaptic plasticity[17] which means potentiating

or depressing synaptic connection in response to received neural signals. The

synaptic plasticity consists of STP, which changes the synaptic connection for short

periods of time, and LTP, which for long periods of time. Until now, the synaptic

plasticity has been emulated in artificial synapses with various mechanisms such as

1

interface energy band modulation, filament formation, phase change, etc.[13-15, 18-22] Notably, most of the artificial synapses have emulated only one type of synaptic plasticity (i.e., either STP or LTP) by one mechanism according to their usage. However, in some biological synapses, STP and LTP do not operate alone, but both work together independently or synergistically giving adaptation for dynamic situations and memory formation at the same time.[23-24]

From this point of view, achieving STP and LTP that operate simultaneously (mixed plasticity) in an artificial synapse can provide the adaptation to dynamic situations and memory formation for the neuromorphic systems that deal with dynamic data. However, it is difficult to achieve the mixed-plasticity with one mechanism, the conventional way to emulate synaptic plasticity, due to the presence of the contradiction issue.[25] For this reason, mixed-plasticity should be achieved by two mechanisms in a device. In a recent study, Sarwat, Syed Ghazi, et al. succeeded in emulating mixed-plasticity reliably and simultaneously in a 3-terminal device by introducing two mechanisms, field effect for STP and phase change for LTP.[25] However, to our knowledge, demonstrations of reliably and simultaneously operated mixed-plasticity by two mechanisms in 2-terminal devices that can provide greater compactness than 3-terminal devices by the absence of one gate terminal are lacking. To achieve vast connectivity and hierarchical structure of synapses with mixed-plasticity, the development of compact 2-terminal devices is

2

essential.

Here, we demonstrated 2-terminal halide perovskite (HP) artificial synapse with mixed-plasticity by adopting ferroelectricity through composition component engineering. At the artificial synapse, we were able to control the behavior of ions and ferroelectric polarization by regulating the magnitude of the applied voltage. Below the coercive voltage (3.5V), it was possible to emulate STP, only halide ion migration occurs. Above the coercive voltage, the effect of the ferroelectric dipole arrangement was dominant. As a result, LTP could be emulated. These separated STP and LTP mechanisms enabled reliably and simultaneously operated mixed-plasticity, which is first demonstration in 2-terminal devices.

Chapter 2. Results and Discussion

2.1. Reasons for Adopting Halide Perovskite

In this work, to implement a 2-terminal artificial synapse with mixed-plasticity, we adopted HP as an active layer due to the following two reasons. i) The HP artificial synapses, which use halide ion migration to emulate plasticity, are STP-dominant devices because of the easy drift and diffusion of halide ions.[13-14] ii) ferroelectric dipoles for LTP which modulate schottky barrier at the HP's interface for a long time can be introduced through HP's composition component engineering. With the long-lasting ferroelectric dipoles and the easy drift and diffusion of halide ions (i.e., ion migration for STP and ferroelectricity for LTP), we could succeed in realizing the reliably and simultaneously operated mixed-plasticity in a 2-terminal artificial synapse.

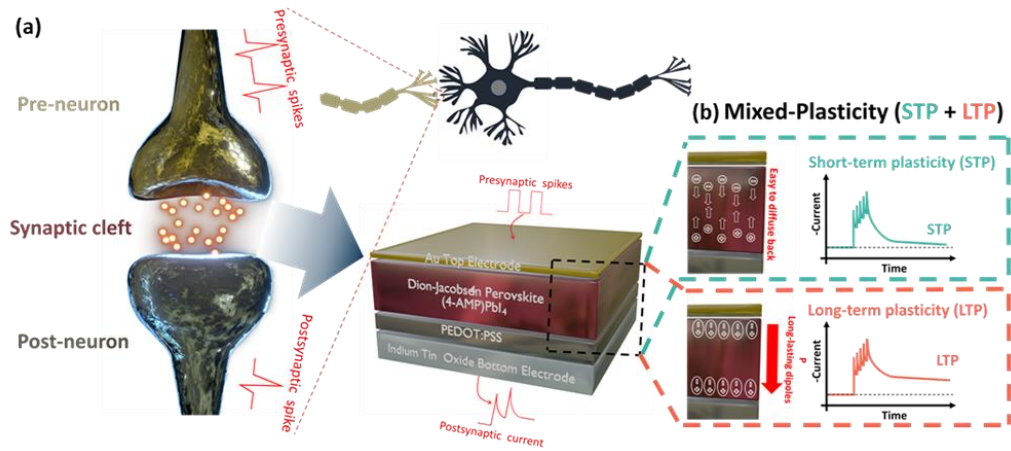## 2.2. Halide Perovskite Artificial Synapse with Mixed-Plasticity (STP + LTP)

The 2-terminal artificial synapse with mixed-plasticity (2-TAM) has the structure of indium tin oxide (ITO) bottom electrode/poly(3,4-ethylenedioxythiophene) polystyrene sulfonate (PEDOT:PSS, Clevios P VP AI4083) buffer layer/2D ferroelectric Dion-Jacobson perovskite (FDJP, note: details will be explained later) active layer/Au top electrode. The Au top electrode emulates the pre-neuron where the presynaptic spikes caused by external stimuli are applied. The ITO bottom electrode/PEDOT:PSS buffer layer emulate the post-neuron where the postsynaptic current is read. The FDJP active layer emulates the synaptic cleft where is the diffuse space of neurotransmitters. This configuration of 2-terminal artificial synapse well emulated several synaptic characteristics (Figure 2) previously reported in perovskite artificial synapses[13-14] by applying presynaptic spikes to the top electrode and reading the postsynaptic current at the bottom electrode (Figure 1a).

In the artificial synapse, we could control STP mode (by the ion migration) and LTP mode (by the ferroelectricity) by regulating the magnitude of the presynaptic spike voltage. When presynaptic spikes (below coercive voltage) are applied to the top electrode, the halide ions or halide vacancies migrate toward the bottom or top electrode's side through the grain boundary. Then, the migrated

halide ions or halide vacancies cause energy band bending in the FDJP active layer to cause conductance change.[26] When the presynaptic spikes are removed to the top electrode, then, the moved halide ions or halide vacancies quickly diffuse back to their original position by concentration gradient difference to cause a quick return of the changed conductance (Figure 3a). Through the quick relaxation process, STP could be emulated. Contrary, when presynaptic spikes (above coercive voltage) are applied to the top electrode, there are field-induced long-lasting ferroelectric dipole arrangements causing long-lasting energy band bending at the end of the FDJP active layer. Even if presynaptic spikes are removed, the long-lasting energy band bending to cause conductance change is remained (Figure 3b). From the long-lasting conductance change, LTP could be emulated in the 2-TAM.

2.3. 2D Dion-Jacobson Perovskite for Suppressing the Migration Distance

In previous reported 3D HP artificial synapses, if the halide ion and vacancy migration distance is long, weak LTP (lasting for tens of minutes) occurs as halide ion or vacancy's trapping at the interface of the perovskites.[13] However, in 2D HP, the 2D structure disturbs the movement of ions and vacancies. As a result, the 2D structure induces short-distance migration of the halide ions and vacancies. In other words, the 2D HP suppresses the occurrence of LTP by preventing the migration induced-trapping at the interface of perovskite.[14] For this reason, we especially adopted 2D HP for the 2-TAM. Among 2D HP, it was theoretically studied that Dion-Jacobson (DJ, ABX_4) phase suppresses the movement of ions and vacancies more than Ruddlesden-Popper (RP, A_2BX_4) phase.[27] As a result, we finally adopted 2D ferroelectric DJ perovskite ((4-AMP)PbI_4) as an active layer for the 2-TAM. (i.e., ion migration only for STP and ferroelectricity only for LTP) Consequently, we could emulate the important mixed-plasticity (STP + LTP) in a single 2-terminal device through the different two mechanisms (Figure 1b).

Figure 1. Schematics of halide perovskite artificial synapse with mixed-plasticity (STP + LTP), a) A biological synapse and a perovskite artificial synapse, b) Mixed-plasticity with STP by ion migration and LTP by ferroelectricity.
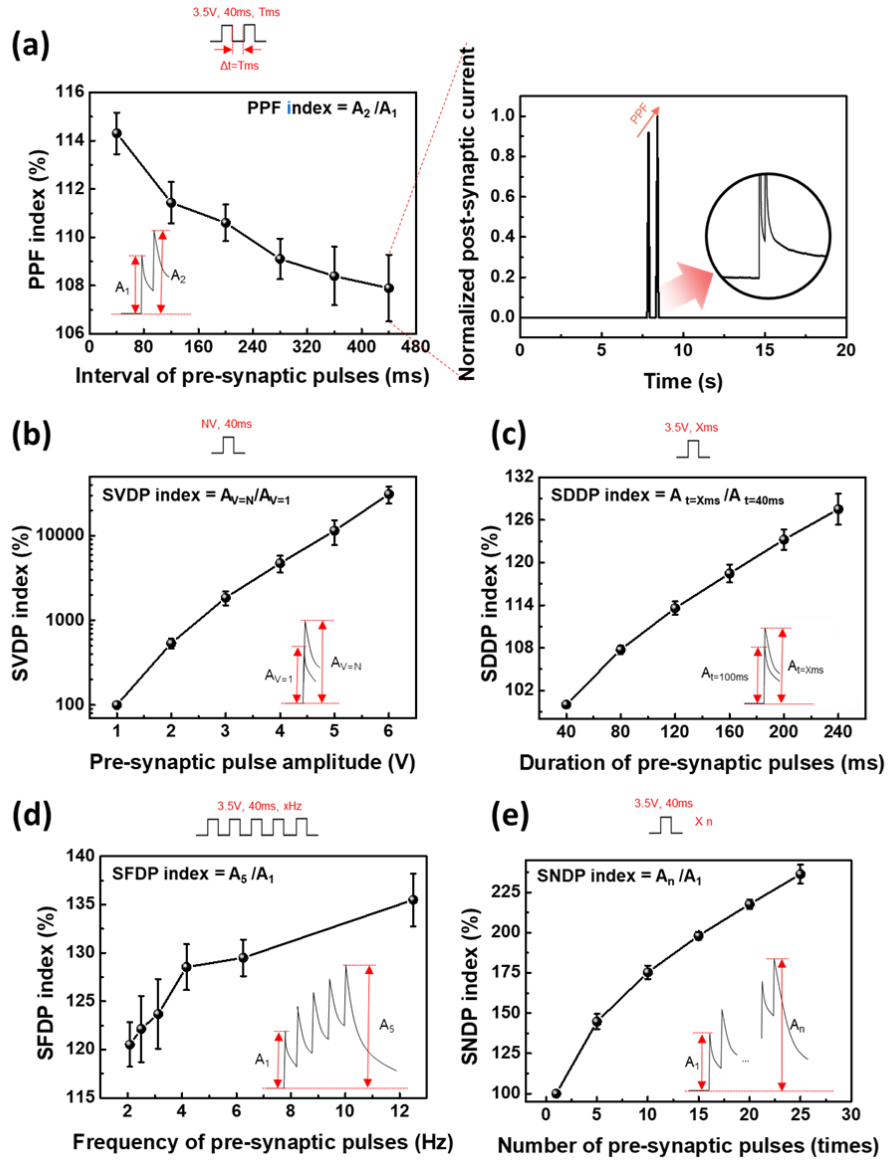
Figure 2. Various synaptic characteristics, a) Paired-pulse facilitation (PPF) index, b) Spike voltage-dependent plasticity (SVDP) index, c) Spike duration-dependent plasticity (SDDP) index, d) Spike frequency-dependent plasticity (SFDP) index, e) Spike number-dependent plasticity (SNDP) index.
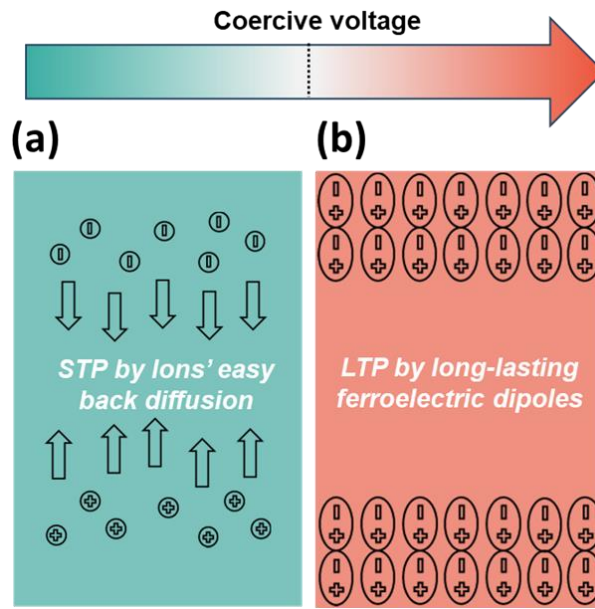
Figure 3. Schematics of mixed-plasticity regulated by the magnitude of the applied voltage, a) STP by ion migration below coercive voltage, b) LTP by ferroelectricity above coercive voltage.

2.4. (4－AMP)PbI₄ Single Crystal Powder Synthesis

4-(aminomethyl)piperidine (4-AMP) was purchased from Sigma-Aldrich. The (4-AMP) was directly used with 57% hydroiodic acid (HI) for preparing (4-AMP)I_2. Then, the (4-AMP)I_2 (185.0 mg, 0.500 mmol) and PbO (111.6 mg, 0.500 mmol) were dissolved in the solution of concentrated HI (57 wt%, 4 mL), followed by the addition of H_3PO_2 (50 wt%, 0.5 mL) in 20 ml vial. The vial was sealed and held at 110°C for 1 hour. After that, the vial was cooled to room temperature for 30 hours or more to obtain an orange single crystal of (4-AMP)PbI₄.

For spin coating the (4-AMP)PbI₄ FDJP thin film, we synthesized (4-AMP)PbI₄ single crystal powder. We compared the (4-AMP)PbI₄ single crystal X-ray diffraction (SC-XRD) with the simulated SC-XRD data to check whether the (4-AMP)PbI₄ single crystal powder was synthesized well or not (Figure 4). The peaks of (4-AMP)PbI₄ SC-XRD are well matched with the simulated data. From this coincidence, we could identify the single crystal powder had properly synthesized. A previous report showed the SC-XRD of (4-AMP)PbI₄ for presenting its monoclinic Pc ferroelectric phase that is essential for ferroelectricity at room temperature.[28] The non-centrosymmetric structure has two 4-AMP molecules, two Pb atoms, and eight I atoms. The 4-AMP cations alternate up and down in the [PbI₄]$^{2-}$ interlayers (Figure 5). Especially, the AMP molecules are located below the centerline dividing the inorganic [PbI4]$^{2-}$ layers along the a-axis. This asymmetric

1 1

structure promotes ferroelectric polarization oriented along the [100] direction

equivalent.

2.5. The (4−AMP)PbI₄ Thin Film Characterization

Through a simple spin-coating process (see Experimental Section), (4-AMP)PbI$_4$ thin film with a thickness of ~80 nm was fabricated (Figure 6) for application to the 2-TAM. To characterize the thin film, we conducted UV–vis absorption spectra measurement (UV-vis). From the UV-vis absorption spectra, we could identify the thin film has 2.34 eV optical band gap from its absorption edge (Figure 7) which is almost consistent with a previously reported paper (ref. = 2.38 eV).[28] To investigate the thin film morphology, we identified scanning electron microscope (SEM) and atomic force microscope (AFM) images. The SEM and AFM images show full coverage on the PEDOT:PSS layer with root-mean-square (RMS) roughness of 9.396 nm (Figure 8a, b). Particularly, to investigate the behavior of ion and vacancy migration, we measured the frequency-dependent capacitance in the frequency range 1 Hz ≤ f ≤ 1 MHz (Figure 9). In the range of 1 Hz ≤ f ≤ 10 Hz, which is a low frequency region, an AC voltage (base DC voltage = 10 mV) with a small amplitude (10 mV ~ 0.5 V) could not induce a significant change in capacitance. The results are presumed that the halide ions and vacancies cannot be moved with the voltage range (10 mV ~ 0.5 V). However, at AC voltage amplitudes of 0.8 V and 1.1 V, the capacitance increases as it moves to the low frequency region. This result indicates that the halide ions and vacancies move clearly above 0.8 V. Consequently, the important point is that at 0.8 V or higher, the

movement of the halide ions and vacancies was clearly observed. As a result, we could implement STP by using the voltage range (0.8 V ~ Coercive voltage). Moreover, to identify the crystallinity of the thin film, we investigated X-ray diffraction (XRD) patterns (Figure 10). From the XRD data ,we could identify a (100) peak located at a low angle which is the origin of ferroelectricity and 2D structure formation.
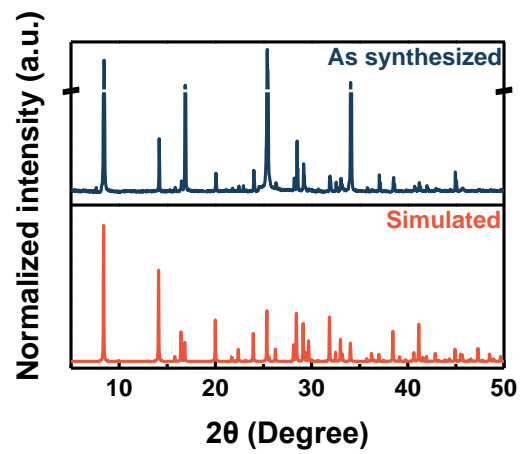
Figure 4. (4-AMP)PbI$_4$ single crystal X-ray diffraction (SC-XRD) data and the simulated SC-XRD data.

A: 4-AMP
B: Pb
X: I

Room-temperature ferroelectric phase
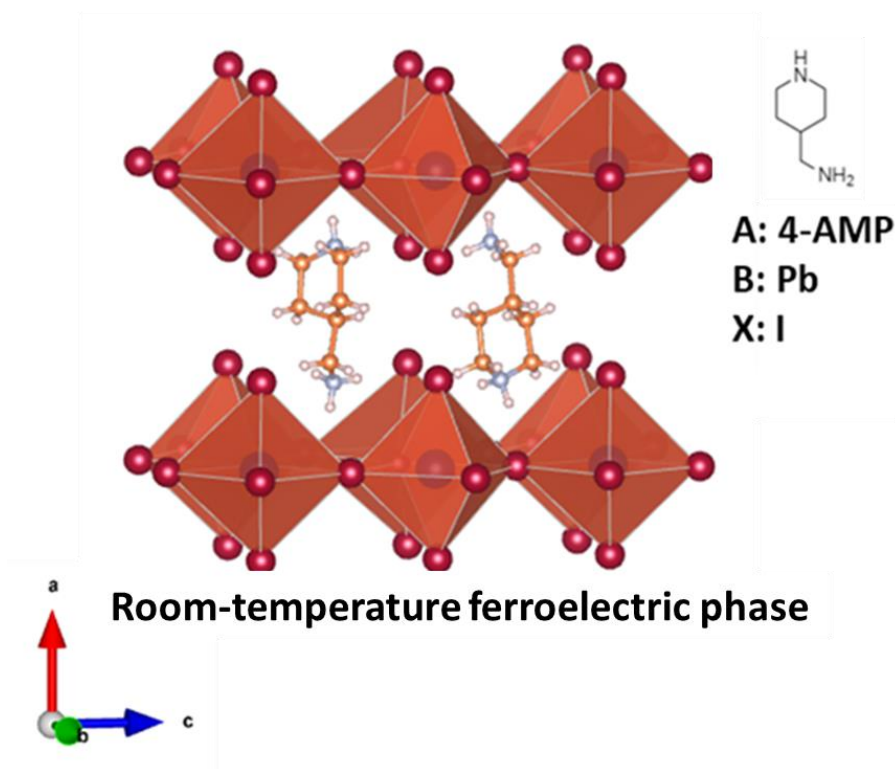
Figure 5. Ferroelectric structure of (4-AMP)PbI$_4$ at 298 K.
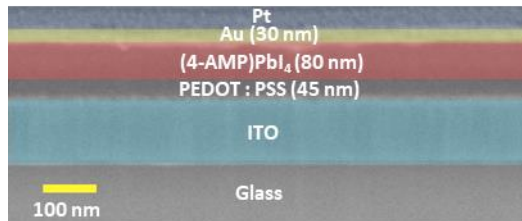
Figure 6. Cross-section scanning electron microscope (SEM) image of the 2-TAM.
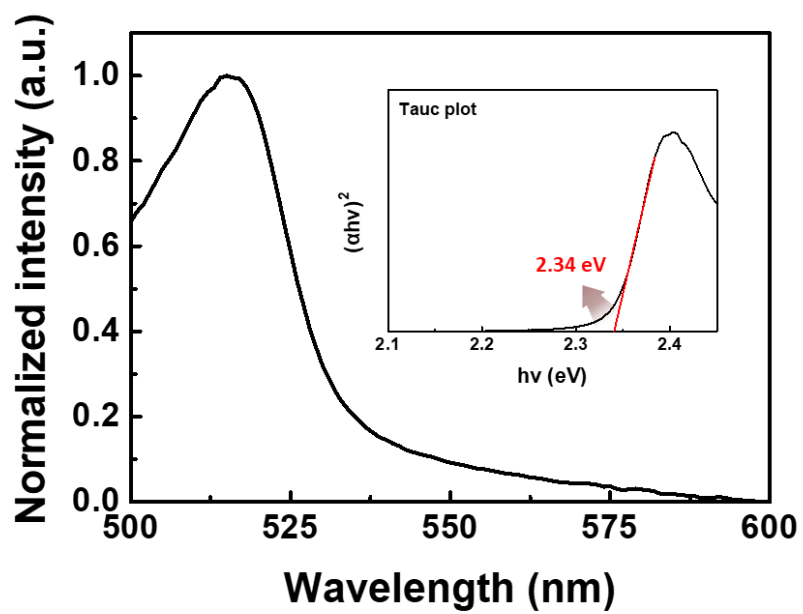
Figure 7. UV–vis absorption spectra of the (4-AMP)PbL$_4$ thin film, Insult: Tauc plot of the absorption spectra.
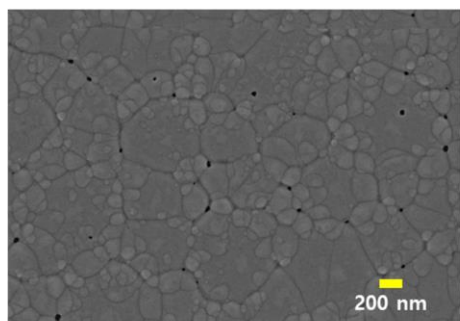
Figure 8. Morphology investigation from a) SEM and b) AFM images of the (4-AMP)PbI$_4$ thin film.

-

19

Figure 9. Capacitance-frequency curve of the (4-AMP)PbI$_4$ thin film.

Figure 10. XRD peaks of the (4-AMP)PbI$_4$ thin film.

2.6. Positive Up Negative Down (PUND) method for Ferroelectric Polarization Measurement

For identifying whether the spin-coated thin film has ferroelectricity, we conducted positive up negative down (PUND) method for polarization measurement.[29-30] The detailed measuring principle of PUND which is the most accurate polar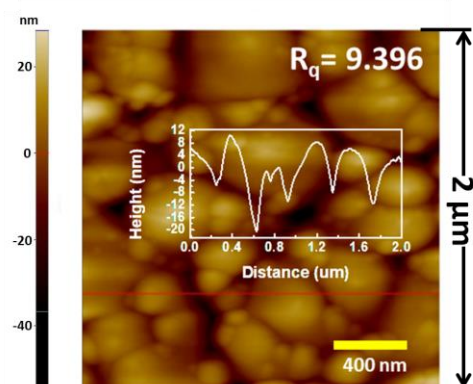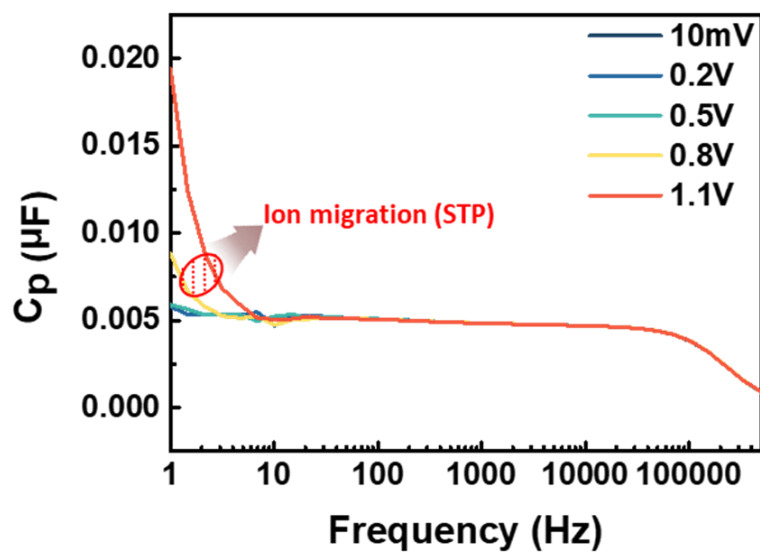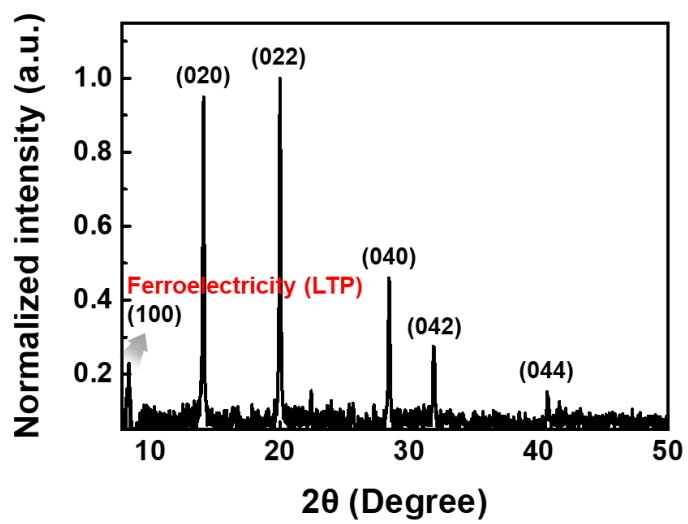ization measurement is introduced in Figure 12. A brief introduction about how to calculate polarization value of the thin film through the PUND measurement is that the sum of the remnant polarization with + sign (P_r) and the remnant polarization with − sign (P^*_r) can be obtained by subtracting the charges per unit area caused by the u pulse (u) from the charges per unit area caused by the p pulse (p). As a result, we could identify $P_r + P^*_r$ (p - u) = 1.09 µc/Cm^2 (Figure 11). Furthermore, we conducted inverse piezo effect investigation through piezo force microscopy (PFM). From the PFM equipment, we could obtain the out-of-plane phase and amplitude mapping image (Figure 13a, b). The histogram in the Figure 13a is a distribution drawn by extracting phase degrees from each pixel in the phase mapping image. The histogram shows a gaussian-like distribution at the -90 degree, which clearly shows that the ferroelectric polarization in the thin film is well-aligned along the vertical direction. If distinct ferroelectric polarization does not exist in the film, the phase distribution should appear evenly across the all phase values.[31-32] Moreover, through the PFM, we could confirm the local

ferroelectric properties of the thin film by measuring the piezoresponse while sweeping from +7 V to -7 V and then back to +7 V (Figure 13c, d). From the Figures 13c, d, we could identify a butterfly shape and a square shape, respectively. These shapes are the results derived from the rapid switching at the coercive voltage where ferroelectric polarization rapidly switches (coercive voltage ≈ -4 V and 3.5 V).[31] From these results in Figure 11, 12, 13, we could confirm that the (4-AMP)PbI$_4$ thin film has ferroelectricity.

2.7. Specification of the PUND Method

PUND measurement is a method widely used to measure the ferroelectric polarization of leaky materials.[29-30] The PUND measurement consists of reset pulse, p pulse, u pulse, n pulse, and d pulse like the Figure 11. The p pulse and u pulse are pulses with a positive sign. The n pulse and d pulse are pulses with a negative sign. Before starting the measurement, the reset pulse is applied to make the device into the P^*_r state. Then, when the p pulse is applied, charges move by the potential difference caused by the p pulse. The total moved charges per unit area caused by the p pulse consist of charges to compensate for dielectric polarization, ferroelectric polarization, and leakage current by the leaky nature of the material. The important point is that the charges for compensating the ferroelectric polarization are the charges for compensating for the polarization switching from the P^*_r to $P_{V=10}$ (saturated polarization). After that, in the u pulse, however, the charges for compensating the ferroelectric polarization are the charges for compensating for the polarization switching from the P_r to the $P_{V=10}$ (Figure 12a).

In practice, the energy band change occurs due to the switching of the ferroelectric polarization. As a result, the leakage current shows a slight difference (Figure 12b). However, PUND measurement ignores this. In other words, leakage currents by the p pulse and u pulse are considered same, although the band change has occurred during the ferroelectric polarization switching. Moreover, PUND

measurement supposes the charges to compensate for dielectric polarization by the p pulse and u pulse also have the same value. It is because dielectric polarization is only affected by the geometrical factors and the material itself. Considering these two conditions, the value of $P_r + P^*_r$ can be obtained by subtracting the charges per unit area caused by the u pulse (u) from the charges per unit area caused by the p pulse (p). In the case of calculating the $P_r + P^*_r$ by using the n pulse and d pulse, we should subtract the charges per unit area caused by the d pulse (d) from the charges per unit area caused by the n pulse (n). In this paper, we did not calculate the $P_r + P^*_r$ through the way using the n and d pulse.

After we had determined, based on the above contents, the shape of the p and u pulses as in the Figure 12b, we conducted PUND measurement while changing the plateau time in the trapezoid-shaped pulses from 5 μs to 10 μs and 20 μs. In the case of 5 μs, the corresponding (4-AMP)PbI$_4$ device did not reach P_s by the p pulse (Figure 12c). In addition, in the case of measuring PUND at 20 μs, there was current increases at the end of the u pulse (Figure 12d). The current increases mean that 20 μs scale is the time scale at which ions start moving at the 10 V. The current increased by this ion migration consequently undervalued the $P_r + P^*_r$ value calculated due to the increased leakage current by the ion migration. As a result of the above reasons, we chose 10 μs, which can reach P_s and is not a time scale for the ion migration (Figure 11).

However, as mentioned the above, the $P_r + P^*_r$ value is slightly under-valued by the energy band change by the ferroelectric polarization switching process, as shown in Figure 12b; the actual $P_r + P^*_r$ value would greater than the calculated value ($P_r + P^*_r$ (p − u) = 1.09 μC/Cm²).
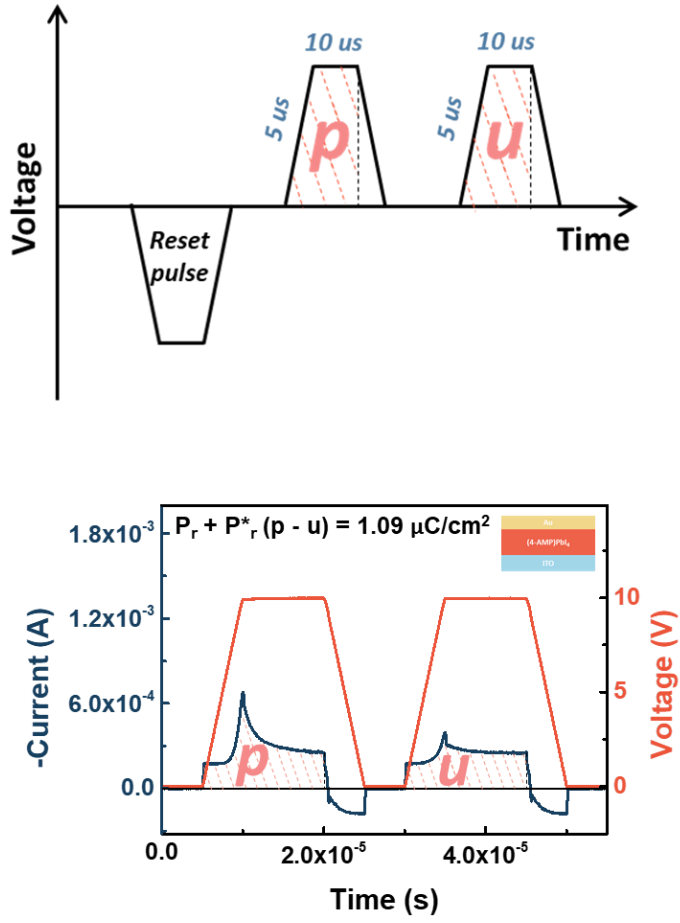
Figure 11. Pulse shapes for PUND measurement and the result of the PUND measurement.
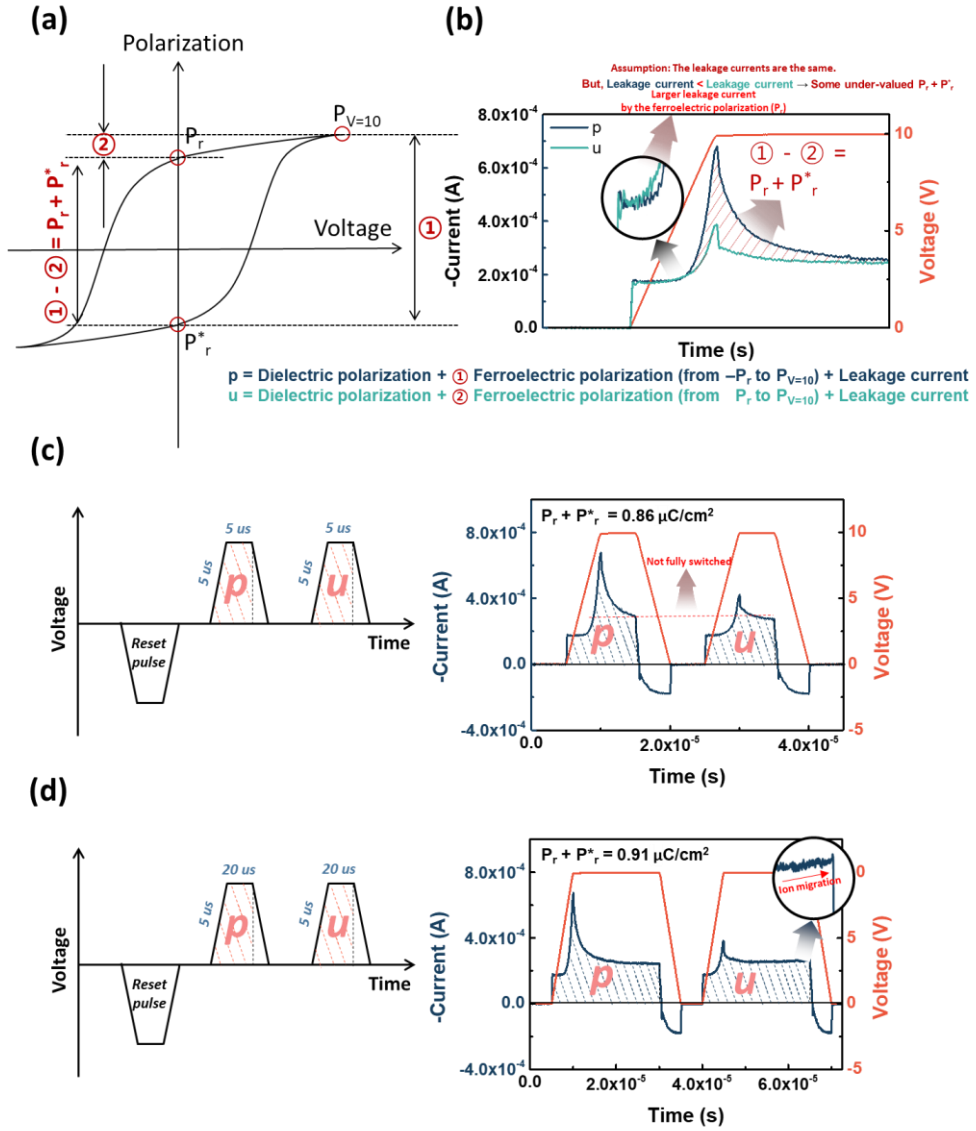
Figure 12. Specification of the PUND measurement, a) Ferroelectric polarization change by the p pulse and the u pulse, b) The PUND measurement's detailed principle, c) 5 µs plateau time in the trapezoid-shaped pulses that cause the ferroelectric polarization to not fully switched, d) 20 µs plateau time in the trapezoid-shaped pulses that cause ion migration to occur.
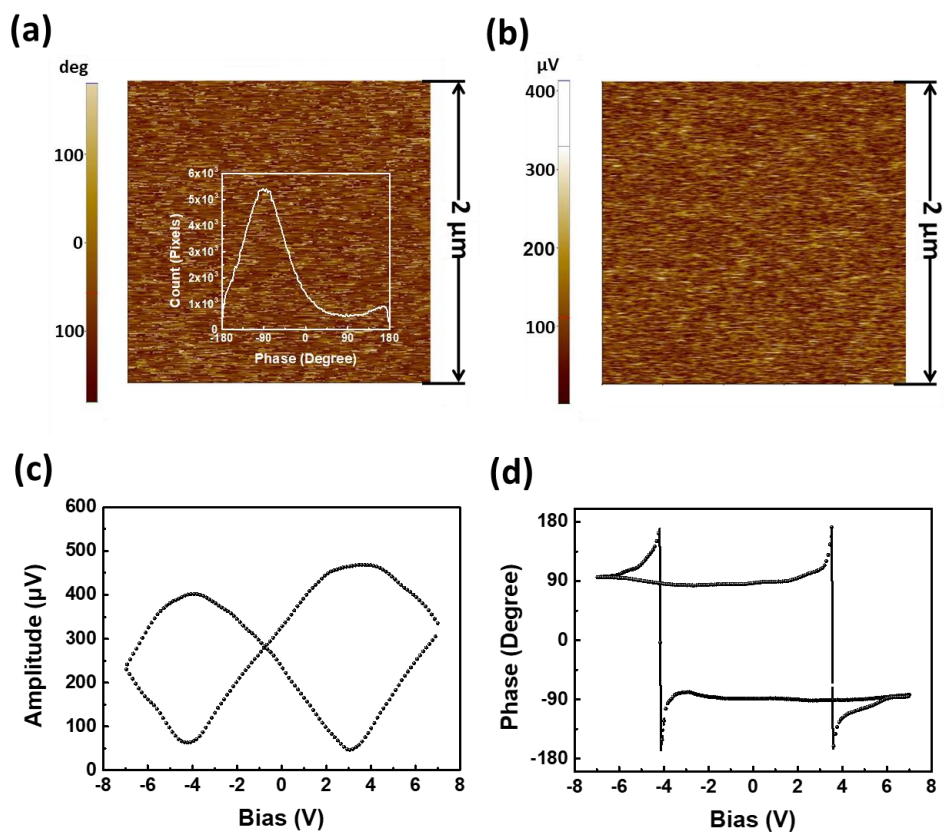
Figure 13. Inverse piezo effect investigation by PFM a) Phase mapping image, Insult: Phase distribution extracted by the phase mapping image, b) Amplitude mapping image, c) Phase hysteresis loop, d) Amplitude hysteresis loop of the (4-AMP)PbI$_4$ thin film.
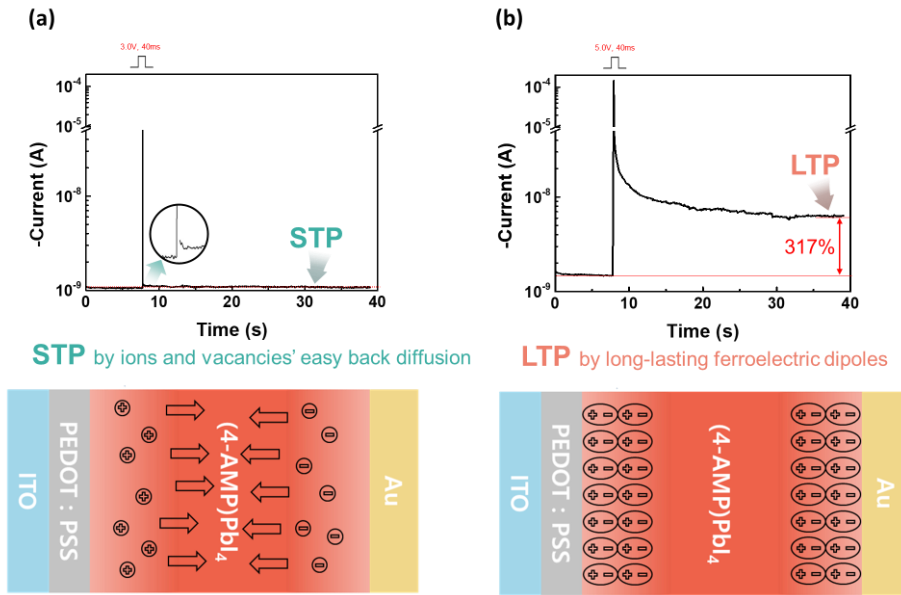
2.8. Mixed-plasticity in the 2-TAM.

To identify whether both STP and LTP can be actually emulated by regulating the magnitude of the voltage (i.e., by the two mechanisms), we applied a presynaptic 3 V spike (STP by halide ion and vacancy migration, below the coercive voltage) and presynaptic 5 V spike (LTP by ferroelectricity, above the coercive voltage) to the top electrode of the 2-TAM. As a result, we could confirm short-term potentiation (STP^*, a type of STP) at the 3 V (Figure 14a) and Long-term potentiation (LTP^*, a type of LTP) at the 5 V (Figure 14b) as expected. Here, to read the synaptic weight, -50 mV, which is weak enough not to affect the 2-TAM, was applied to the bottom electrode. In other words, the synaptic weight can be tracked by reading the postsynaptic current through the bottom electrode being applied at -50 mV. In addition, to confirm how the transition between STP^* and LTP^* occurs according to the presynaptic spike voltage magnitude, we increased the presynaptic spike voltage from 0.5 V to 4.5 V in 0.5 V increment while comparing the baseline (i.e., synaptic weight) at 0 second before the voltage was applied and the baseline at 40 seconds, 22 seconds after the presynaptic spike was applied. Consequently, we could find that at 3.5 V, this $I_{baseline=0s}/I_{baseline=40s}$ ratio increased (set voltage, Figure 15). Before we investigated the case of depression, we had identified whether the depression plasticity worked well or not (Figure 16). From the Figure 16, we could identify that the depression plasticity works well.

Then, as in the case of potentiation, we applied presynaptic spike voltage from -1 V to -5 V in -0.5 V decrement to the top electrode while comparing the baseline at 0 seconds before the voltage was applied and the baseline at 40 seconds, 22 seconds after the presynaptic spike was applied ($I_{baseline=0s}/I_{baseline=40s}$, Figure 17). From the $I_{baseline=0s}/I_{baseline=40s}$ ratio of the depression case, we could find that $I_{baseline=0s}/I_{baseline=40s}$ ratio decrease at -4V (reset voltage). Afterwards, with the set voltage and reset voltage obtained in this way, we compared it with the coercive voltage obtained through PFM (Figure 18). As a result, we could identify the coincidence of the values (i.e., (re)set voltage ≈ coercive voltage). From this coincidence, we could conclude that the transition from STP to LTP at set voltage and reset voltage is due to the ferroelectric polarization switching. Clearly, the migration of ions and vacancies also occurs in LTP. However, the migrated components diffuses back rapidly, leaving only the switched ferroelectric dipoles that consequently cause LTP.

Figure 14. Mixed-plasticity (STP +LTP) of the 2-TAM, a) STP by ions and vacancies' easy back diffusion below the coercive voltage, b) LTP by long-lasting ferroelectric dipoles above the coercive voltage.
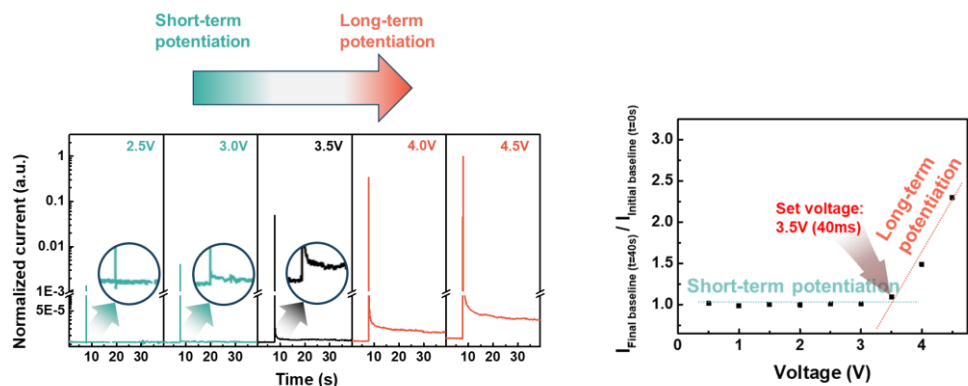
Figure 15. Transition from STP[*] to LTP[*] at the set voltage.
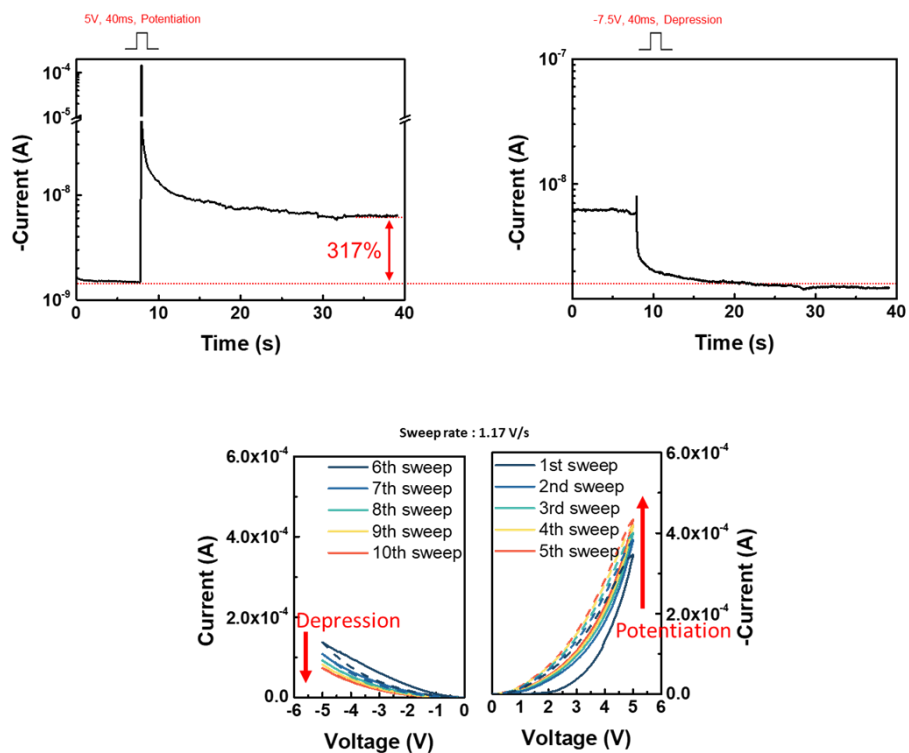
Figure 16. Potentiation and depression of the 2-TAM.

3 4

Figure 17. Transition from short-term depression to long-term depression at the reset voltage.

Figure 18. Transition from STP and LTP at (re)set voltage and phase hysteresis loop obtained by PFM.

Chapter 3. Conclusion

We have demonstrated a two-terminal artificial synapse with mixed-plasticity by two mechanisms that can provide adaptation to dynamic situation and memory formation for handling real-time data. To achieve the two mechanisms in a device, we adopted halide perovskite as active layer of the 2-terminal artificial 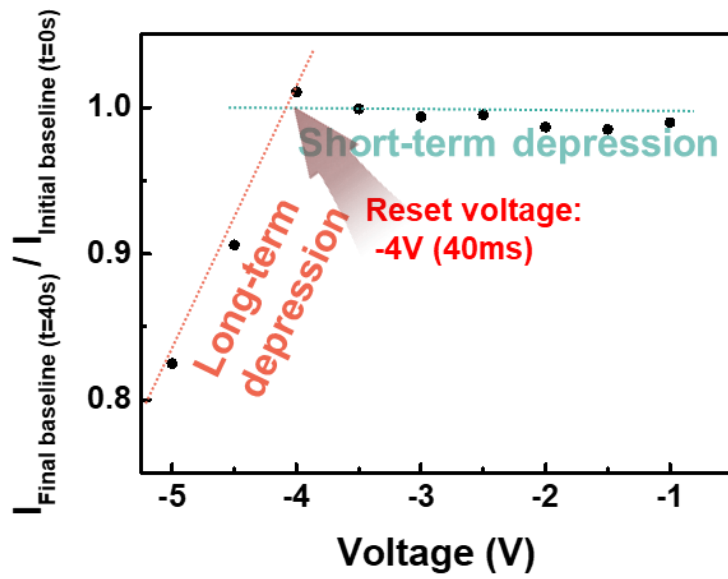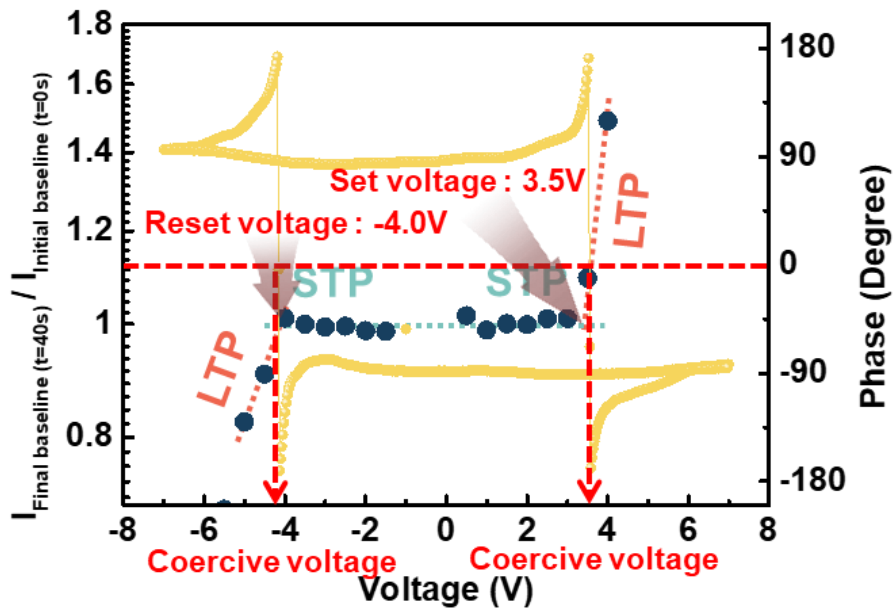synapse. Moreover, we introduced ferroelectricity through A-site composition component engineering into the halide perovskite active layer. By combining the intrinsic STP by the ion and vacancy migration of the halide perovskite and LTP by the introduced ferroelectricity, we could achieve the mixed-plasticity in a 2-terminal device by two mechanisms. Especially, we adopted 2D DJ phase halide perovskite as an active layer due to the feature of suppressing the occurrence of LTP (i.e., STP only by ion migration and LTP only by ferroelectricity). As a result, we demonstrated STP at a voltage lower the coercive or set voltage and LTP at a voltage higher than the coercive or set voltage; we showed controlling the STP mode and LTP mode by regulating the presynaptic spike voltage magnitude. In addition, we demonstrated that both STP and LTP operate well simultaneously and reliably.

Chapter 4. Experimental Section

Device Fabrication: ITO-sputtered glass or p+Si substrates were cleaned by sonicator in acetone and 2-propanol. Then, UV-ozone treatment was applied to make the hydrophobic substrates hydrophilic. With the hydrophilic substrates, PEDOT:PSS (Clevios P VP AI4083) was spin-coated on the substrates and annealed at 150°C for 30 minutes. After the PEODT:PSS deposition, (4-AMP)PbI$_4$ was spin-coated onto the PEDOT:PSS thin film and baked at 100 °C for 10 min in a glovebox. Then, 30 nm thick rectangular Au metal dots were thermally deposited through a shadow mask in a high vacuum chamber (<10^{-6} Torr).

Measurements: UV–vis absorption spectra was measured using a UV–vis absorption spectrophotometer (Cary-5000). Scanning electron microscopy (SEM) image was obtained using a field-emission SEM (SUPRA 55VP) at the National Instrumentation Center for Environmental Management. Atomic force microscopy (AFM) image was obtained using a NX-10 at the Research Institute of Advanced Materials. Capacitance–frequency characteristics were measured using an electrochemical impedance spectroscopy (SP-200). X-ray diffraction was conducted using a D8 Advance at the Research Institute of Advanced Materials. Positive up negative down (PUND) measurement is conducted using a Keithly 4200A-SCS. Inverse piezo effect was investigated using a NX-10 at the Research

Institute of Advanced Materials. All electrical characteristics of the devices were measured using a Keysight B1500A semiconductor parameter analyzer in a nitrogen atmosphere.

Bibliography

[1] V. M. Ho, J.-A. Lee, K. C. Martin, *Science* **2011**, 334, 623.

[2] K. Roy, A. Jaiswal, P. Panda, *Nature* **2019**, 575, 607.

[3] D. J. Felleman, D. C. Van Essen, *Cerebral cortex (New York, NY: 1991)* **1991**, 1, 1.

[4] E. Bullmore, O. Sporns, *Nature reviews neuroscience* **2012**, 13, 336.

[5] Y. Lee, H.-L. Park, Y. Kim, T.-W. Lee, *Joule* **2021**, 5, 794.

[6] Y. Lee, Y. Liu, D.-G. Seo, J. Y. Oh, Y. Kim, J. Li, J. Kang, J. Kim, J. Mun, A. M. Foudeh, *Nature Biomedical Engineering* **2022**, 1.

[7] G.-T. Go, Y. Lee, D.-G. Seo, M. Pei, W. Lee, H. Yang, T.-W. Lee, *Advanced Intelligent Systems* **2020**, 2, 2000012.

[8] W. Xu, S.-Y. Min, H. Hwang, T.-W. Lee, *Science advances* **2016**, 2, e1501326.

[9] D.-G. Seo, Y. Lee, G.-T. Go, M. Pei, S. Jung, Y. H. Jeong, W. Lee, H.-L. Park, S.-W. Kim, H. Yang, *Nano Energy* **2019**, 65, 104035.

[10] Y. Lee, J. Y. Oh, W. Xu, O. Kim, T. R. Kim, J. Kang, Y. Kim, D. Son, J. B.-H. Tok, M. J. Park, *Science advances* **2018**, 4, eaat7387.

[11] H. L. Park, H. Kim, D. Lim, H. Zhou, Y. H. Kim, Y. Lee, S. Park, T. W. Lee, *Advanced Materials* **2020**, 32, 1906899.

[12] W. Xu, T. L. Nguyen, Y.-T. Kim, C. Wolf, R. Pfattner, J. Lopez, B.-G. Chae, S.-I. Kim, M. Y. Lee, E.-Y. Shin, *Nano Energy* **2018**, 48, 575.

[13] W. Xu, H. Cho, Y. H. Kim, Y. T. Kim, C. Wolf, C. G. Park, T. W. Lee, *Advanced Materials* **2016**, 28, 5916.

[14] S. I. Kim, Y. Lee, M. H. Park, G. T. Go, Y. H. Kim, W. Xu, H. D. Lee, H. Kim, D. G. Seo, W. Lee, T. W. Lee, *Advanced Electronic Materials* **2019**, 5.

[15] S. Choi, S. H. Tan, Z. Li, Y. Kim, C. Choi, P.-Y. Chen, H. Yeon, S. Yu, J. Kim, *Nature materials* **2018**, 17, 335.

[16] S. Jung, H. Lee, S. Myung, H. Kim, S. K. Yoon, S.-W. Kwon, Y. Ju, M. Kim, W. Yi, S. Han, *Nature* **2022**, 601, 211.

[17] Y. Humeau, D. Choquet, *Nature neuroscience* **2019**, 22, 1536.

[18] S. Oh, T. Kim, M. Kwak, J. Song, J. Woo, S. Jeon, I. K. Yoo, H. Hwang, *IEEE Electron Device Letters* **2017**, 38, 732.

[19] M.-K. Kim, J.-S. Lee, *Nano letters* **2019**, 19, 2044.

[20] M. Suri, O. Bichler, D. Querlioz, O. Cueto, L. Perniola, V. Sousa, D. Vuillaume, C. Gamrat, B. DeSalvo, presented at *2011 International Electron Devices Meeting*, **2011**.

[21] S. B. Eryilmaz, D. Kuzum, R. Jeyasingh, S. Kim, M. BrightSky, C. Lam, H.-S. P. Wong, *Frontiers in neuroscience* **2014**, 8, 205.

[22] J. H. Yoon, Z. Wang, K. M. Kim, H. Wu, V. Ravichandran, Q. Xia, C. S. Hwang, J. J. Yang, *Nature communications* **2018**, 9, 1.

[23] S. Cassenaer, G. Laurent, *Nature* **2007**, 448, 709.

[24] F. Fiebig, A. Lansner, *Journal of Neuroscience* **2017**, 37, 83.

[25] S. G. Sarwat, B. Kersting, T. Moraitis, V. P. Jonnalagadda, A. Sebastian, *Nature Nanotechnology* **2022**, 17, 507.

[26] Y. Zhao, C. Liang, H. Zhang, D. Li, D. Tian, G. Li, X. Jing, W. Zhang, W. Xiao, Q. Liu, *Energy & Environmental Science* **2015**, 8, 1256.

[27] Z. Xu, M. Chen, S. F. Liu, *The Journal of Physical Chemistry Letters* **2019**, 10, 3670.

[28] I.-H. Park, Q. Zhang, K. C. Kwon, Z. Zhu, W. Yu, K. Leng, D. Giovanni, H. S. Choi, I. Abdelwahab, Q.-H. Xu, *Journal of the American Chemical Society* **2019**, 141, 15972.

[29] A. Grigoriev, M. M. Azad, J. McCampbell, *Review of Scientific Instruments* **2011**, 82, 124704.

[30] E. Parsonnet, Y.-L. Huang, T. Gosavi, A. Qualls, D. Nikonov, C.-C. Lin, I. Young, J. Bokor, L. W. Martin, R. Ramesh, *Physical review letters* **2020**, 125, 067601.

[31] D. Seol, G. S. Han, C. Bae, H. Shin, H. S. Jung, Y. Kim, *Journal of Materials Chemistry A* **2015**, 3, 20352.

[32] Y.-J. Kim, T.-V. Dang, H.-J. Choi, B.-J. Park, J.-H. Eom, H.-A. Song, D. Seol, Y. Kim, S.-H. Shin, J. Nah, *Journal of Materials Chemistry A* **2016**, 4, 756.

Abstract

단기 가소성(STP)과 장기 가소성(LTP)이 동시에 작동하는 인공 시냅스(혼합 가소성)를 달성하면 동적 상황에 대한 적응과 기억 형성을 동시에 제공할 수 있습니다. 따라서 단일 장치에서 혼합 가소성(STP + LTP)을 구현하면 실시간 데이터를 처리하는 뉴로모픽 시스템의 구현에 기여할 수 있습니다. 혼합 가소성을 구현하는 여러 장치가 있지만 이러한 장치에서는 STP 와 LTP 가 단일 메커니즘으로 제어됩니다. 단일 메커니즘으로 혼합 가소성을 제어하는 것은 모순 문제의 존재로 인해 어려운 일이므로 이 문제를 해결하기 위해 여기서는 2 단자 인공 시냅스의 활성층으로 할라이드 페로브스카이트를 채택했습니다. 또한 조성 성분 공학을 통해 그 할라이드 페로브스카이트 활성층에 강유전성을 도입했습니다. 그 결과, 그 할라이드 페로브스카이트 활성층에서 할라이드 페로브스카이트의 이온 및 공공 이동을 STP 구현을 위해 그리고 도입된 강유전성을 LTP 구현을 위해 활용할 수 있었습니다. 즉 안정적이고 동시에 작동하는 혼합 가소성을 위해 2 개의 분리된 메커니즘을 이용할 수 있었습니다. 결과적으로 우리는 위와 같은 새로운 접근 방식을 통해 안정적이고 동시에 작동하는 혼합 가소성을 구현하는 데 성공하였습니다.

학번 : 2020_22900